SPE 80444

An Integrated Sand Control Method Evaluation

Ariffin Samsuri, SPE, S.H. Sim, and C.H. Tan, University of Technology, Malaysia

This paper was prepared for presentation at the SPE Asia Pacific Oil and Gas Conference and Exhibition held in Jakarta, Indonesia, 15–17 April 2003.

Abstract

A numerical model has been developed that is able to predict the onset of sand production and evaluate the performance of sand control, should sand production becomes unavoidable. The simulation of perforation stability was carried out first using a two-dimensional, two-phase finite-element model. This is a coupled geomechanical and fluid flow model. The rock was assumed to be heterogeneous and the pores were completely filled with fluid. The deformation condition is considered as plane strain and either the Mohr-Coulomb or Drucker-Prager yield surface was used to designate perforation failure. The model enables the study on the effect of perforation pattern and density on wellbore stability. Simulation runs on a sample model indicated that the lowest pore pressure, the greatest shear stress and minor principle stress were found close to the perforation tip. The greatest major principle stress occured around the center of perforation roof. In other words, the perforation was always surrounded by high stress concentration. In those events when sand production is a certainty, it is necessary to evaluate the performance of sand control methods to be used. A finite-difference flow model was used to calculate the additional pressure drop from the well boundary to the sand control screen. The Forchheimer equation was used in place of the more conservative Darcy equation so that the effect of high-velocity flow to the well performance could be considered. The result of several sample runs indicated firm relationship between total additional pressure drop and the flow rate imposed, where a larger flow rate will cause greater pressure loss. Also, the well productivity showed improvement with more shots per foot. The results suggested that the majority of well pressure drop was caused by the casing-cement tunnel.

Development of numerical model

In an integrated approach to sand production problems, we seek to predict the stress state around the wellbore for different operating conditions, and if sanding is inevitable, the optimum gravel-pack configuration is chosen. The tools involved are a coupled mechanical-fluid flow model and a three-dimensional well productivity model. The essential equations for the two models are given below.

The Perforation Stability Prediction Model

In predicting the perforation stability, the borehole is divided into slices. The number of slices depends on the thickness of each slice and the borehole radius. The deformation condition for every slice is considered to be of plane-strain type and the oil flow is confined within the domain of each slice. The perforation is assumed to be a cylinder with an open end, the other end being semi-spherical. **Fig. 1** shows a slice with one perforation cavity. The interactions between slices are considered by taking into account the stress component that act between the slices.

Generally, the perforation stability prediction model is comprised of 2 main elements: flow continuity equation and solid equilibrium equation. The flow continuity equations calculate the fluid pressure distribution around perforation, while solid equilibrium equation determine the stress state and rock deformation. According to Lewis and Schrefler (1987), the flow continuity equation is:

$$-\nabla^{\mathrm{T}}\left\{\mathbf{k}\frac{k_{r_l}}{\mu_l B_l}\nabla\left(p_l+\rho_l g h\right)\right\}+\lambda_A\frac{\partial p_o}{\partial t}+\lambda_B\frac{\partial p_w}{\partial t}+\frac{S_l}{B_l}\left(\mathbf{m}^{\mathrm{T}}-\frac{\mathbf{m}^{\mathrm{T}}\mathbf{D}_{\mathrm{T}}}{3K_s}\right)\frac{\partial\epsilon}{\partial t}=0 \qquad \text{..... (1)}$$

The solid equilibrium equation can be written as:

$$\int_\Omega \delta\epsilon^{\mathrm{T}}\mathbf{D}_{\mathrm{T}}\frac{\partial\epsilon}{\partial t}\mathrm{d}\Omega+\int_\Omega \delta\epsilon^{\mathrm{T}}\left(\frac{\mathbf{D}_{\mathrm{T}}\mathbf{m}}{3K_s}-\mathbf{m}\right)\overline{\mathrm{SO}}\frac{\partial p_o}{\partial t}\mathrm{d}\Omega+\int_\Omega \delta\epsilon^{\mathrm{T}}\left(\frac{\mathbf{D}_{\mathrm{T}}\mathbf{m}}{3K_s}-\mathbf{m}\right)\overline{\mathrm{SW}}\frac{\partial p_w}{\partial t}\mathrm{d}\Omega-\int_\Omega \delta\epsilon^{\mathrm{T}}\mathbf{D}_{\mathrm{T}}\frac{\partial\varepsilon_o}{\partial t}\mathrm{d}\Omega-\int_\Omega \delta\mathbf{u}^{\mathrm{T}}\frac{\mathrm{d}\mathbf{b}}{\mathrm{d}t}\mathrm{d}\Omega-\int_\Gamma \delta\mathbf{u}^{\mathrm{T}}\frac{\mathrm{d}\hat{\mathbf{t}}}{\mathrm{d}t}\mathrm{d}\Gamma=0 \qquad \text{.....(2)}$$

Eq. (1) and (2) are coupled and solved by using the finite-element method (FEM). $\mathbf{D}^{\mathrm{T}}$ in Eqs. (1) and (2) is the tangential stiffness matrix which is defined by a constitutive model. It can be the tangential elastic stiffness matrix, $\mathbf{D}^{\mathrm{e}}$ for elastic deformation or the tangent elastoplastic modulus matrix $\mathbf{D}^{\mathrm{ep}}$ for plastic deformation. Two types of elastoplastic models

suitable for the prediction of perforation failure are the Mohr-Coulomb yield surface and the Drucker-Prager yield surface, and both are available in this model (Veeken et al., 1991; Brady, 1994).

Gravel-Packed Well Productivity Model

The governing equation for one-phase flow through a petroleum reservoir in three-dimensional cylindrical co-ordinates (r,θ,z) is

$$\frac{1}{r}\frac{\partial}{\partial r}\left[r\delta_r\lambda R\left(\frac{\partial P}{\partial r}-\gamma\frac{\partial h}{\partial r}\right)\right]+\frac{1}{r^2}\frac{\partial}{\partial\theta}\left[\delta_\theta\lambda\theta\left(\frac{\partial P}{\partial\theta}-\gamma\frac{\partial h}{\partial\theta}\right)\right]+\frac{\partial}{\partial z}\left[\delta_z\lambda Z\left(\frac{\partial P}{\partial z}-\gamma\frac{\partial h}{\partial z}\right)\right]=\Psi\frac{\partial P}{\partial t}+q \quad \text{.....(3)}$$

The governing equation is discretized in space in the directions of r, θ and z for both the oil and water phases. The governing equation is also discretized in time using the forward difference approach. In this work, the distinction between the perforation and the reservoir rock is in their permeability where gravel permeability is used for the gravel-filled perforations and original permeability for the reservoir.

The IMPES (Implicit Pressure Explicit Saturation) method is used to combine the governing equations for the oil and water phases. The difference equations are written for each grid block and the resulting system of equations is collected and expressed in matrix form. The matrix is solved using the iterative Gauss-Seidel method for the pressure at the innermost part of the perforation, i.e. P_p. It should be noted that perforation here refers to the part of the perforation outside the casing. The pressure drop across this zone is the difference between the reservoir pressure, P_r, and P_p.

High-velocity flow effects

As the flow velocity increases, deviations from Darcy's Law are observed. In this study, the Forchheimer equation is used in place of Darcy's Law in the modeling equations. The Forchheimer equation is given as

$$u=-\delta\frac{k}{\mu}\frac{dp}{dx} \quad \text{.....(4)}$$

where

$$\delta=\frac{1}{\left(1+\frac{\beta\rho k}{\mu}|u|\right)} \quad \text{.....(5)}$$

The symbol δ is a turbulence correction factor, which is introduced into the governing equation that is Eq. 3. Another parameter important in high-velocity flow is the high-velocity coefficient β as found in Eq. 5. Among the numerous correlations available in the literature, the Brown (1984) correlation is popular and is used in this work. The Brown (1984) correlation gives β as a function of permeability, that is

$$\beta=\frac{1.47\times10^7}{k^{0.55}} \quad \text{.....(6)}$$

Pressure drop in the casing-cement tunnel

In this work, the perforation is divided into two sections. The first is the perforation in the formation outside the casing, which has been discussed in the previous section. The second is a shorter tunnel in the both the casing and the cement. Due to its relatively small size, the flow regime in this tunnel is regarded as linear. The equation for linear one-dimensional flow through a perforation is given by Saucier (1974) as

$$\Delta P_{pf}=0.888\frac{L\mu qB}{kA}+9.1\times10^{-13}\beta L\rho\left(\frac{qB}{A}\right)^2 \quad \text{.....(7)}$$

The first term on the right side gives the pressure drop due to Darcy flow and the second term represent the additional pressure drop due to high-velocity flow. The parameter β is the same high-velocity coefficient as presented in Eq.5.

Result and discussion

The applicability of the perforation prediction model is demonstrated by running a sample case. This sample model was run for 495.01 second. Five slices were used to construct a perforation. Relevant data of the sample model are given in **Table 1**. While **Table 2** shows the formation volume factor for the oil in the sample model.

Fig. 2 and **Fig. 3** shows the pore pressure distribution at nodal points along the perforation roof for q = 0.01328 m^3/D/perf and q = 0.02655 m^3/D/perf. When the production rate is increased the pore pressure is decreased due to more oil withdrawal and rock compaction. The difference in pore pressure between the sand face and the wellbore outer boundary is very small for both production rates because the model is small. Both figures indicate that along the perforation roof, pore pressure is very low and the lowest pore pressure is at the zone close to the perforation tip.

Fig. 4 shows the stress distribution at Gauss point salong the perforation roof for 2 different production rates (0.01328 m^3/D/perforation and 0.02655 m^3/D/perforation). From this figure, for both production rates, the greatest shear stress and minor principle stress were always located at around the perforation tip. On the other hand, the major principle stress was highest around the center of perforation roof. This figure also suggests that the perforation was always surrounded by high stress concentration. If the production rate is increased, the stresses along the perforation roof will also increase. This is because a higher production rates will induce larger displacements that cause increase in stress.

As with the wellbore stability model earlier, a case study is performed using the well productivity model. A fictitious model is constructed based on the design of a typical well installed with an inside-casing gravel pack. The model has a cylindrical shape with a hole at the center. For simplicity, the model is assumed to contain only oil. The model is delineated on the outside, top and bottom by no-flow boundaries. The hole at the center of the model acts as the wellbore. The number of grids used is 5 in the radial (r), 12 in the angular (θ) and 12 in the vertical (z) directions, respectively, giving a total of 720 gridblocks. Both cases of

openhole and perforation flow were considered. The basic condition of a drawdown test is simulated with the flow rate being kept constant. The duration of all simulation runs was 1 hr. (3600s), which is approximately the time required to reach pseudo-steady state. The *additional* pressure drop due to gravel-packed perforations outside the casing for a particular perforated case, ΔP_{perf}, is obtained by subtracting the pressure at the opening of the perforation (perforated case) from the pressure at the same position for the openhole case. For the subsequent linear flow through the casing-cement tunnel, the additional pressure drop, ΔP_{tun}, is calculated directly from Eq. 5. The total additional pressure drop is the sum of the two.

The total additional pressure drop in a gravel-packed well is shown in **Fig. 5** for different perforation densities and flow rates. As expected, the total additional pressure drop decreased with more shots per foot. This is consistent with earlier studies of productivity of perforated wells (Locke,1981; McLeod, 1983), which suggested better productivity with higher shot densities. Also, the total additional pressure drop was found to increase with flow rate. The effect of flow rate on total pressure drop was greater for lower shot densities. This is most probably due to high-velocity flow that is more evident in wells having lower shot densities.

Fig. 6 shows the contribution of gravel-packed perforations outside the casing and the casing-cement tunnels to the total additional pressure drop. For all flow rates and shot densities studied, most of the pressure drop occurred in the casing-cement tunnels. The pressure drop in casing-cement tunnels accounted for 89-95% of the total additional pressure drop. This is especially the case in high-permeability reservoirs, where the combined effect of perforation and well geometry will be small compared to the casing-cement tunnels. In gravel-packed wells in such reservoirs, it is likely that the total pressure drop will be dominated by pressure losses in the casing-cement tunnels. However, in low permeability reservoirs, or reservoirs that experience severe damage (due to drilling fluids invasion, crushed zone etc.), the effect of gravel-packed perforation outside the casing may contribute more to the total pressure drop. As can be seen in **Fig. 6**, the contribution of perforations outside the casing increased with increasing shot density, which is true for all the flow rates studied.

Conclusion

Based on the results presented thus far, the following conclusions are drawn:

1. The perforation stability prediction model is able to determine pore pressure distribution and stress state for the rock around the perforation. With these information, perforation failure can be predicted by using one of the two failure criterions given.
2. An increase in flow rate will cause higher stresses to exist around perforation, and thus increase the likelihood of perforation failure.
3. The well productivity model can be used to determine the productivity of gravel-packed wells under different operating conditions.
4. The productivity of gravel-packed wells is improved with increasing perforation densities; higher flow rates will cause greater pressure loss and thus impair well productivity.
5. The majority of well pressure drop is due to pressure loss in the casing-cement tunnel.

Acknowledgments

The authors wish to thank the Ministry of Science, Technology and the Environment, Malaysia for providing the necessary funding that made this study possible.

Nomenclature

$C_{rm} = \frac{(1-\phi)}{K_s} - \frac{1}{(3K_s)^2}\mathbf{m}^T\mathbf{D}_T\mathbf{m}$

$\overline{SO} = S_o - p_o S_w' + p_w S_w'$

$\overline{SW} = S_w + p_o S_w' - p_w S_w'$

$\left(\frac{1}{B_o}\right)'$ - slope of $\left(\frac{1}{B_o}\right)$ versus p_o curve

$\left(\frac{1}{B_w}\right)'$ - slope of $\left(\frac{1}{B_w}\right)$ versus p_w curve

B - formation volume factor
b - body force
$\mathbf{D}_T$ - tangent matrix
g - gravity
h - the head above some arbitrary datum
k - absolute permeability matrix of the medium
k_r - relative permeability function
K_s - bulk modulus of solid phase
m - for normal stress components is unity and for shear stress components is zero
p - fluid pressure
q - production rate
S - fluid saturation
S_w' - slope of the capillary curve
t - time level
$\hat{\mathbf{t}}$ - boundary traction
$\delta\mathbf{u}$ - virtual displacement
$\boldsymbol{\varepsilon}$ - total strain of rock skeleton
ε_o - autogeneous strain
ϕ - porosity
$\lambda_A = \lambda_{oo}$ or λ_{ow}
$\lambda_B = \lambda_{wo}$ or λ_{ww}

$\lambda_{oo} = -\frac{\phi}{B_o}S_w' + \phi S_o\left(\frac{1}{B_o}\right)' + \frac{S_o}{B_o}C_{rm}\overline{SO}$

$\lambda_{ow} = \frac{\phi}{B_w}S_w' + \frac{S_w}{B_w}C_{rm}\overline{SO}$

$\lambda_{wo} = \frac{\phi}{B_o}S_w' + \frac{S_o}{B_o}C_{rm}\overline{SW}$

$$\lambda_{ww} = -\frac{\phi}{B_w}S_w' + \phi S_w\left(\frac{1}{B_w}\right)' + \frac{S_w}{B_w}C_{rm}\overline{SW}$$

μ - dynamic viscosity
ρ - density
Γ - boundary
Ω - domain
u - fluid velocity
δ - turbulence factor
Ψ - $\frac{\phi}{B}$, dimensionless
β - high-velocity β coefficient
L - length of casing-cement tunnel
A - flow area of perforation tunnel

Subscript
o - oil phase
w - water phase

Superscript
T - matrix transpose

References

1. Aziz, K., Settari, A. (1979). "Petroleum Reservoir Simulation." Elsevier Applied Science.
2. Brady, B.H. (1994). "Some Recent Advances in Computational Geomechanics for Energy Resource Recovery." *Computer Methods and Advances in Geomechanics*, Siriwardane and Zaman (eds), Balkema Rotterdam. 21-31.
3. Brown, K.E. (1984). "The Technology of Artificial Lift Methods." PennWell Books, Tulsa.
4. Firoozabadi, A. and Katz, D.L. (1979). "An Analysis of High-velocity Gas Flow through Porous Media.," *Journal of Petroleum Technology*, Society of Petroleum Engineers.
5. Golan, M., Whitson, C.H. (1991). "Well Performance." Second Edition, Prentice-Hall Inc., New Jersey.
6. Lewis, R.W. and Schrefler, B.A. (1987). "The Finite Element Method in the Deformation and Consolidation of Porous Media." Chichester: John Wiley and Sons.
7. Locke, S. (1981). "An Advanced Method for Predicting the Productivity Ratio of a Perforated Well." SPE 8804
8. McLeod, H.O. (1983). "The Effect of Perforating Conditions on Well Performance." SPE 10649.
9. Pucknell, J.K. and Mason, J.N.E. (1992). "Predicting the Pressure Drop in a Cased-Hole Gravel Pack Completion." SPE 24984
10. Saucier, R.J. (1974) "Considerations in Gravel-Pack Design." *Journal of Petroleum Technology*. Society of Petroleum Engineers.
11. Unneland, T. (2001) "Performance of High-Rate Gravel-packed Oil Wells." Dr. Techn. Thesis, Norwegian University of Science and Technology.
12. Veeken, C.A.M., Davies, D.R., Kenter, C.J. and Kooijman, A.P. (1991). "Sand Production Prediction Review: Developing an Integrated Approach." SPE 22792.

Appendices

Table 1: Data for perforation stability prediction model

Model outer radius	1.524 m
Wellbore radius	0.1524 m
Model height	0.3048 m
Young's modulus	1.030×10^{7} Pa
Poisson's ratio	0.38
Friction angle	20°
Porosity	25%
Absolute permeability	1.9738×10^{-7} m^2
Initial pressure	1.3790×10^{7} m^2
Oil viscosity	2.3×10^{-3} Pa.s
Oil density	8.5×10^{2} E+03 kg/m^3
Perforation length	0.1921 m
Perforation diameter	0.0636 m

Table 2: Formation volume factor for perforation stability prediction model

Pressure (MPa)	Bo
8.2737	1.2543
9.6527	1.2498
11.0316	1.2453
12.4106	1.2408
13.7895	1.2363
15.1685	1.2318
16.5474	1.2273
17.9264	1.2228

Table 3: Data for gravel-packed well productivity model

Model outer radius	9.1440 m
Wellbore radius	0.1524 m
Model height	0.3048 m
Porosity	35%
Perforation length	0.1130 m
Perforation diameter	0.0254 m
Perforation density	Openhole, 4 SPF, 6 SPF and 12 SPF
Phasing angle	90° (4 SPF), 60° (6 SPF) and 30° (12 SPF)
Gravel permeability	1.8111×10^{-5} m^2
formation permeability	4.9350×10^{-7} m^2
Initial pressure	1.3790×10^{7} Pa
Oil viscosity	6.50×10^{-3} Pa.s
Oil density	782.20 kg/m^3
Flow rates	794.94 m^3/D, 1589.87 m^3/D and 3179.75 m^3/D

Table 4: Formation volume factor for gravel-packed well productivity model

Pressure (Pa)	B_o
1.38×10^7	1.700
1.34×10^7	1.640
1.31×10^7	1.600
1.28×10^7	1.570
1.24×10^7	1.561
1.21×10^7	1.550
1.17×10^7	1.547
1.14×10^7	1.543
1.10×10^7	1.540

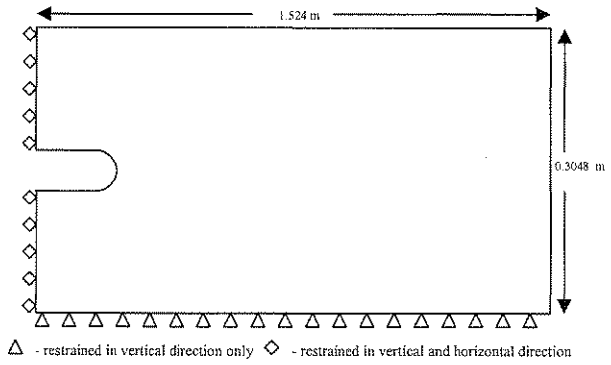

Figure 1: Perforation model

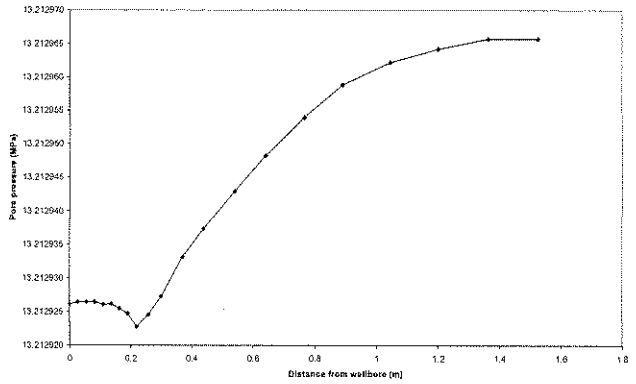

Figure 2: Pore pressure distribution along perforation roof ($q = 0.01328$ m^3/D/perf)

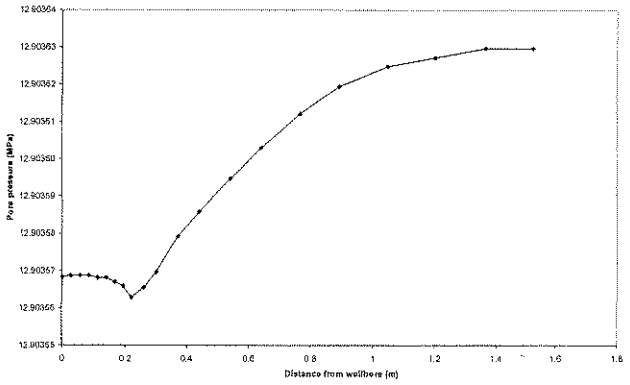

Figure 3 : Pore pressure distribution along perforation roof ($q = 0.02655$ m^3/D/perf)

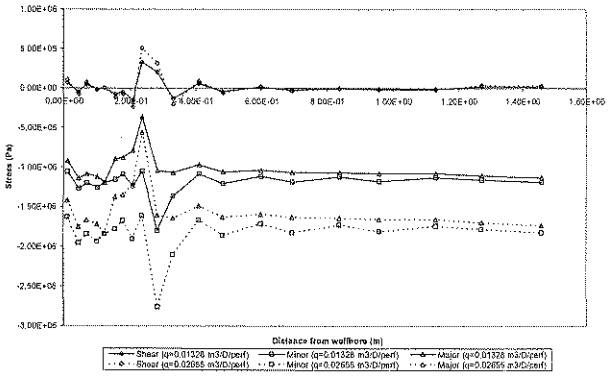

Figure 4: Stress distribution along perforation roof.

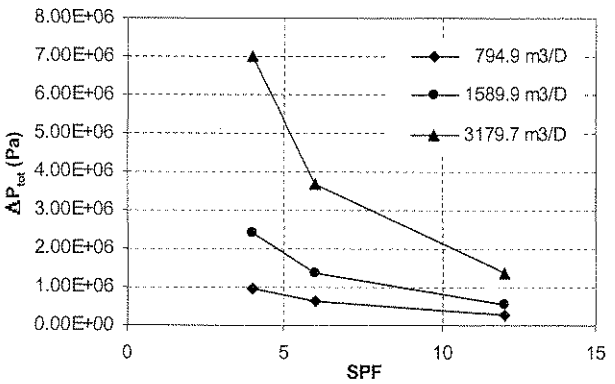

Figure 5 : The effect of perforation density and flow rate on total additional pressure drop

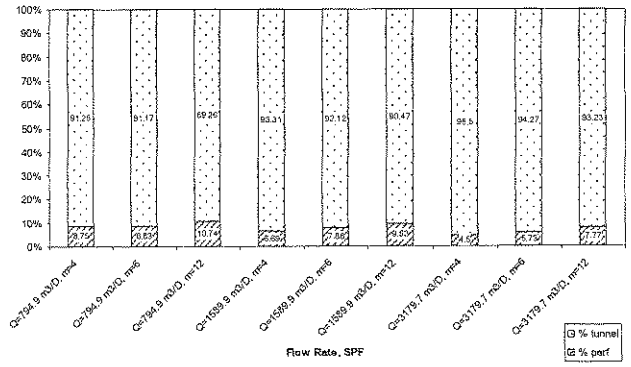

Figure 6 : The contribution of gravel-packed perforation (beyond casing) and casing-cement tunnel on total additional pressure drop